doi: 10.82124/CEAS-GNC-2026-060 CEAS-GNC-2026-060

A hybrid navigation control solution for autonomous approach and landing of an airliner in GPS-denied environment

Gustav Öman Lundin Research Engineer, ONERA - The French Aerospace Lab, Information Processing and Systems Department, 31000, Toulouse, France. gustav.oman_lundin@onera.fr

Sofiane Kraïem Research Engineer, ONERA - The French Aerospace Lab, Information Processing and Systems Department, 31000, Toulouse, France. sofiane.kraiem@onera.fr

Mathieu Brunot Research Engineer, Airbus, 31000, Toulouse, France. mathieu.brunot@airbus.com

Augustin Fuchs Research Engineer, ONERA - The French Aerospace Lab, Information Processing and Systems Department, 31000, Toulouse, France. augustin.fuchs@onera.fr

Cédric Seren Research Engineer, ONERA - The French Aerospace Lab, Information Processing and Systems Department, 31000, Toulouse, France. cedric.seren@onera.fr

ABSTRACT

Modern aircraft navigation relies heavily on Global Navigation Satellite Systems (GNSS) for both en-route and approach operations. However, the inherent vulnerability of civil GNSS signals to interference underscores the necessity of Alternative Position, Navigation, and Timing (APNT) solutions. This work investigates the integration of GNSS, Distance Measuring Equipment (DME), Inertial Reference System (IRS), Visual sensors, and Air Data Reference (ADR) within two navigation filter architectures: a tightly coupled design exploiting raw GNSS observations, and a loosely coupled design based on GNSS-derived position and velocity. A dedicated filter is further developed for estimating DME measurement biases. Performance is evaluated using real flight data with simulated permanent and intermittent GNSS outages. In parallel, a comprehensive DME error model is proposed, combining Gaussian-distributed nominal errors with transient multipath effects. The error model is subsequently integrated into a previously presented Pose-Based Visual Servoing (PBVS) strategy, and the control approach is validated on a real-time simulation platform during en-route, approach, and landing phases. The results demonstrate the feasibility of robust APNT navigation through hybrid architectures, while establishing an analytical foundation for the integration of DME error models into advanced navigation and control frameworks.

Keywords: Autonomous vehicles, Multisensor Data Fusion (MDF), Adaptive Extended Kalman Filtering (AEKF)

Nomenclature

Coordinates and Frames

λ, ϕ, h	=	Longitude, latitude, altitude
E, N, B, T	=	Earth, Navigation, Body, Terrestrial frames
$R_{A,B}$	=	Rotation matrix from frame B to frame A

$\vec{e}_i$ = Unit vector along axis i
ψ, θ, φ = Euler angles (heading, pitch, roll)
s_*, c_* = $\sin(*)$, $\cos(*)$

States and Kinematics

$\vec{P}_E, \vec{V}_E$ = Position and velocity in Earth frame
$\vec{B}_{A,B}$ = Accelerometer bias (Body frame)
$\vec{X}$ = Navigation filter state vector
$\vec{g}$ = Local gravity vector
$\vec{\omega}_T$ = Earth rotation rate (Terrestrial frame)
$\vec{A}_B, \vec{A}_{B,m}$ = True and measured body accelerations
$\vec{n}_{B,m}$ = Measured body-frame load factor

Noise and Uncertainty Models

$\vec{v}_{A,B}, \vec{v}_{B_{A,B}}, \vec{v}_{n,B}$ = Accelerometer, bias, and load factor noises
$\vec{v}_{b_{DME},t_k}$ = DME bias process noise at time t_k
$V_{t_k}, W_{t_{k+1}}$ = Process and measurement noise covariance matrices
$\sigma_{A_{B,i}}, \sigma_{B_{A,B,i}}$ = Std. dev. of accel. and bias random walk
$\sigma_{z_p}, \sigma_{\rho_{DME_j}}$ = Pressure altitude and DME range std. dev.
$\vec{\gamma}, S_\gamma$ = Kalman innovation vector and covariance
n_σ = Confidence level (number of std. dev.)

DME and Bias Estimation

ρ_{DME_j} = DME range to station j
$b_{DME_j}, \bar{b}_{DME}$ = Estimated and maximum DME bias
τ_b = DME bias correlation time constant
N_{eq} = Equivalent stochastic gain (bias saturation)
P_{b_j,t_k} = Bias variance at time t_k
$t_b, Y_{t_k - t_b}$ = Bias appearance time and Heaviside function
ϕ_{t_b,t_k} = Fault signature vector
$F_{b,t_k}, G_{b,t_k}, H_{b,t_{k+1}}$ = Bias filter state-space matrices
ε_{DME} = DME measurement error (noise + bias)

Control and Guidance Variables

DEVLOC, DEVGLD = Localizer and glide deviations
LTP = Landing Threshold Point (deviation reference)

1 Introduction

Modern aircraft navigation relies primarily on Global Navigation Satellite Systems (GNSS) for both en-route and precision approach operations. Although GNSS provides global coverage and high positioning accuracy, it's inherently vulnerable to jamming, spoofing, and unintentional interference. These vulnerabilities raise significant concerns in aviation, where the continuity, availability, and integrity of navigation services are critical.

To mitigate these limitations, the concept of *Alternative Position, Navigation, and Timing* (APNT) has emerged. APNT encompasses a range of heterogeneous technologies, including ground-based navigation aids such as Distance Measuring Equipment (DME) and VHF Omnidirectional Range (VOR) [1], satellite communication constellations such as Iridium—whose signals may be secondarily exploited for positioning—and opportunistic terrestrial sources such as 4G and 5G mobile networks [2]. Over the past decade, renewed research has focused on developing non-GNSS-based positioning methods to enhance navigation robustness [3]. The backbone of current APNT architectures remains ground-based radio infrastructure, particularly DME, Instrument Landing System (ILS), and other wide-area antenna networks [3]. The objective of APNT is to provide reliable positioning throughout climb, cruise, and approach phases, ensuring compliance with Required Navigation Performance (RNP) 1.0 in cruise and

0.3 in climb and arrival. Moreover, APNT must guarantee not only positional accuracy but also integrity monitoring, constraining the navigation solution in both precision and reliability. Classical navigation systems are typically based on Bayesian filtering approaches such as the Kalman filter or particle filters [4–7], which can adapt to varying noise conditions. However, these methods rely on stochastic error models and generally lack formal convergence guarantees unless the system is uniformly observable or transformed accordingly. Alternative filters based on nonlinear stability theory [8–10] address this issue, though at the cost of increased tuning complexity [11, 12].

The core of the presented work builds upon classical sensor fusion principles, integrating DME range and pressure altitude measurements into an inertial navigation framework. Such integration has been explored since the early days of avionics [13, 14] and remains an active research area [15–18]. A flaw in the works in this domain remains the error model of the DME, which is consistently very conservative since it is based on regulations rather than actual observed signal-in-spae errors. A large class of APNT solutions can also be categorized under *Navigation by Signals of Opportunity* ((NAV)SOP) [19, 20], which exploits signals from non-navigation sources such as cellular towers, broadcast antennas, or low-Earth orbit (LEO) communication satellites. As shown in [21], such signals can support navigation even at altitudes up to 23,000 ft, achieving accuracies from a few meters to several tens of meters depending on constellation geometry and signal quality [3, 21]. While DME-based systems typically offer fewer but longer-range measurements compared to SOPs, both approaches share a common philosophy—estimating the state from partial range or angle observations. Beyond accuracy, integrity monitoring remains essential to quantify estimation confidence, often expressed through protection levels that bound the maximum estimation error given a fixed integrity risk [22, 23].

The main contributions of this paper are threefold. First, we develop and evaluate two hybrid navigation filter architectures that integrate GNSS, DME, Inertial Reference System (IRS), visual sensors, and Air Data Reference (ADR): a tightly coupled filter exploiting raw GNSS observations and a loosely coupled filter using GNSS-derived states. Second, we propose a comprehensive DME error model that combines Gaussian-distributed nominal noise with transient multipath effects. Third, we integrate this DME error model into a previously developed Pose-Based Visual Servoing (PBVS) strategy [24] and validate the overall hybrid navigation and control framework using a real-time simulation platform [25] across en-route, approach, and landing phases. These contributions collectively demonstrate the feasibility of robust APNT navigation and provide new insights into visual-assisted, safety-critical aircraft operations.

The remainder of this paper is structured as follows. Section 2 introduces the DME error model derived from real flight data. Section 3 presents the integration of DME measurements into the Multisensor Data Fusion (MDF) framework. Section 4 describes the hybrid PBVS strategy and evaluates system performance under realistic environmental conditions. Finally, Section 5 concludes the paper and outlines perspectives for future work.

2 DME Model Identification

2.1 DME Measurement Principle

DME range measurements are derived from time-of-flight pseudoranges. The aircraft (interrogator) computes the time difference between the transmission of an interrogation pulse and the reception of the transponder reply, subtracting a nominal 50 μs response delay, as illustrated in Fig. 1. The DME measurement process consists of three steps: 1) The aircraft transmits a request signal (ping) and records the transmission time $T_{\mathrm{Tx},1}$. 2) Any DME ground station within range responds 50 μs after receiving the signal, transmitting its identifier in 4-digit ASCII. 3) The aircraft receives the reply at $T_{\mathrm{Rx},2}$, measures the

response frequency, and computes the pseudorange $\rho_{DME,i}$ to the i-th DME station as:

$$\rho_{DME} = c\,\frac{T_{\mathrm{Rx},1} - T_{\mathrm{Tx},2} - 50\ \mu s}{2} \tag{1}$$

where c is the speed of light.

The dominant error sources in the measured time-of-flight are tropospheric delay and multipath effects [26–28]. Tropospheric delay generally induces nearly constant biases on the order of tens of meters, whereas multipath introduces transient errors reaching several hundred meters [29]. Additional contributions may arise from interrogator or transponder clock drift; for instance, a 1 ns clock error produces a 15 cm range bias.

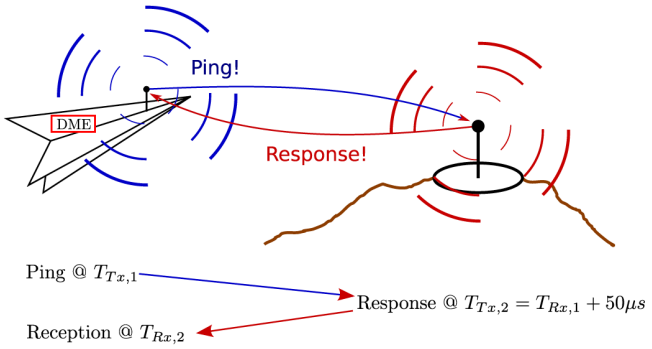

Fig. 1 DME functional principle

This study focuses on navigation errors arising from DME signal-in-space range inaccuracies rather than the internal DME processing itself. To quantify such errors, a theoretical reference range between the aircraft and the DME station is required. As shown in Fig. 2b, this range is computed in the Earth-Centered, Earth-Fixed (ECEF) frame (E-frame). Fig. 2a illustrates the different reference frames used. Transformation between frames is handled through standard rotation matrices. Conversion from the NED (North-East-Down) frame to the body frame (B-frame) involves rotation by the Euler angles (φ, θ, ψ):

$$R_{N,B}(\varphi,\theta,\psi) = \begin{pmatrix} \mathrm{c}_\theta \mathrm{c}_\psi & \mathrm{s}_\varphi \mathrm{s}_\theta \mathrm{c}_\psi - \mathrm{c}_\varphi \mathrm{s}_\psi & \mathrm{s}_\varphi \mathrm{s}_\psi + \mathrm{c}_\varphi \mathrm{s}_\theta \mathrm{c}_\psi \\ \mathrm{c}_\theta \mathrm{s}_\psi & \mathrm{s}_\varphi \mathrm{s}_\psi \mathrm{s}_\theta + \mathrm{c}_\varphi \mathrm{c}_\psi & -\mathrm{s}_\varphi \mathrm{c}_\psi + \mathrm{c}_\varphi \mathrm{s}_\psi \mathrm{s}_\theta \\ -\mathrm{s}_\theta & \mathrm{s}_\varphi \mathrm{c}_\theta & \mathrm{c}_\varphi \mathrm{c}_\theta \end{pmatrix}. \tag{2}$$

Transformation from the E-frame to the N-frame involves rotations about longitude λ and latitude ϕ:

$$R_{E,N}(\lambda,\phi) = \begin{pmatrix} -\mathrm{s}_\phi \mathrm{c}_\lambda & -\mathrm{s}_\lambda & -\mathrm{c}_\phi \mathrm{c}_\lambda \\ -\mathrm{s}_\phi \mathrm{s}_\lambda & \mathrm{c}_\lambda & -\mathrm{c}_\phi \mathrm{s}_\lambda \\ \mathrm{c}_\phi & 0 & -\mathrm{s}_\phi \end{pmatrix}. \tag{3}$$

Given a vector $\boldsymbol{r}_E$ in the E-frame, its expression in the B-frame is:

$$\vec{\boldsymbol{r}}_B = R_{B,N} R_{N,E} \vec{\boldsymbol{r}}_E = R_{B,E} \vec{\boldsymbol{r}}_E \tag{4}$$

For rotation matrices, it holds that $R_{x,y}^T = R_{x,y}^{-1} = R_{y,x}$ and $R_{x,y} R_{x,y}^T = I$.

The position in the E-frame (X, Y, Z) can be derived from geodetic coordinates (λ, ϕ, z) using the WGS-84 ellipsoid:

$$\begin{aligned} X &= (N + z)\,\mathrm{c}_\lambda\,\mathrm{c}_\phi \\ Y &= (N + z)\,\mathrm{c}_\lambda\,\mathrm{s}_\phi \\ Z &= [(1 - e^2)N + z]\,\mathrm{s}_\lambda \\ N &= \frac{a}{\sqrt{1 - e^2 \mathrm{s}_\lambda^2}} \end{aligned} \tag{5}$$

where $a = 6{,}378{,}137$ m and $e = 0.081819190842622$ are the WGS-84 constants.

The inverse transformation is given by the extremely accurate approximation:

$$\begin{aligned} \tan\lambda &= Y/X \\ \tan\phi &= \frac{Z + \varepsilon b \mathrm{s}_u^3}{X - e^2 a \mathrm{c}_u^3} \\ z &= X\sec\phi - \nu \end{aligned} \tag{6}$$

where $\tan u = (Z/X)(a/b)$ and ν is the radius of curvature in the prime vertical for latitude ϕ [30].

Using this transformation, the position vectors of the aircraft and DME station are given by $\vec{r}_{A/C}$ and $\vec{r}_{DME,i}$ respectively. The theoretical range between them is:

$$\rho_{A/C,DME} = \|\vec{r}_{A/C} - \vec{r}_{DME,i}\| \tag{7}$$

and the corresponding range error:

$$\varepsilon_{DME} = \rho_{DME,i} - \rho_{A/C,DME} \tag{8}$$

The following section develops an empirical DME error model based on flight data using Equations 7 and 8.

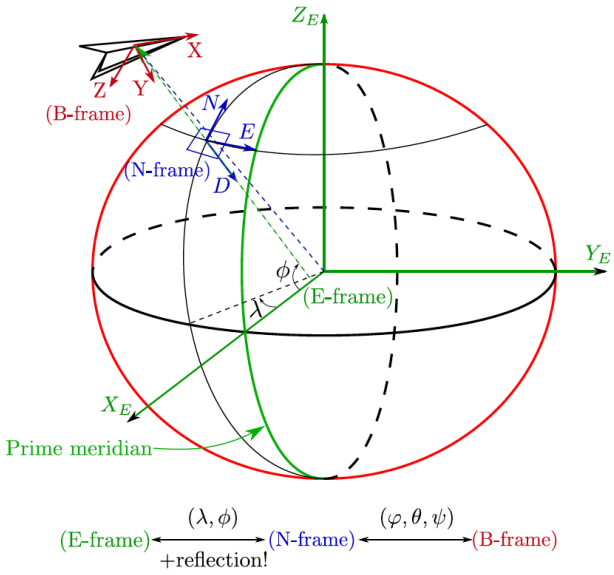

(a) The E-, N-, and B-frames

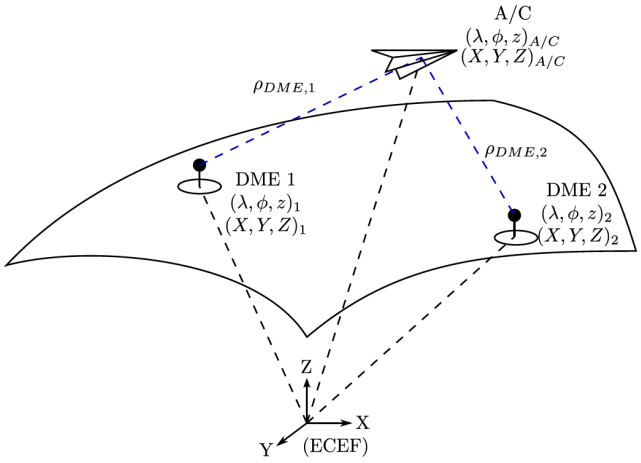

(b) DME and aircraft in the E-frame

2.2 DME Error Model

The previous subsection described the DME measurement principle and the computation of theoretical ranges in the ECEF frame. This subsection focuses on characterizing the stochastic behavior of DME measurements from flight data to derive a representative error model suitable for integration into a multisensor navigation filter.

The range error $\varepsilon_{DME}(t)$ is modeled as the combination of a quasi-static bias, a transient multipath component, and a filtered zero-mean noise process:

$$\varepsilon_{DME}(t) = b_{DME}(t) + \int_0^t w(\tau)h(t-\tau)d\tau + b_{MP}(t), \tag{9}$$

where $h(t)$ is a shaping filter describing noise coloration. This decomposition isolates different error sources for both estimation and integrity analysis.

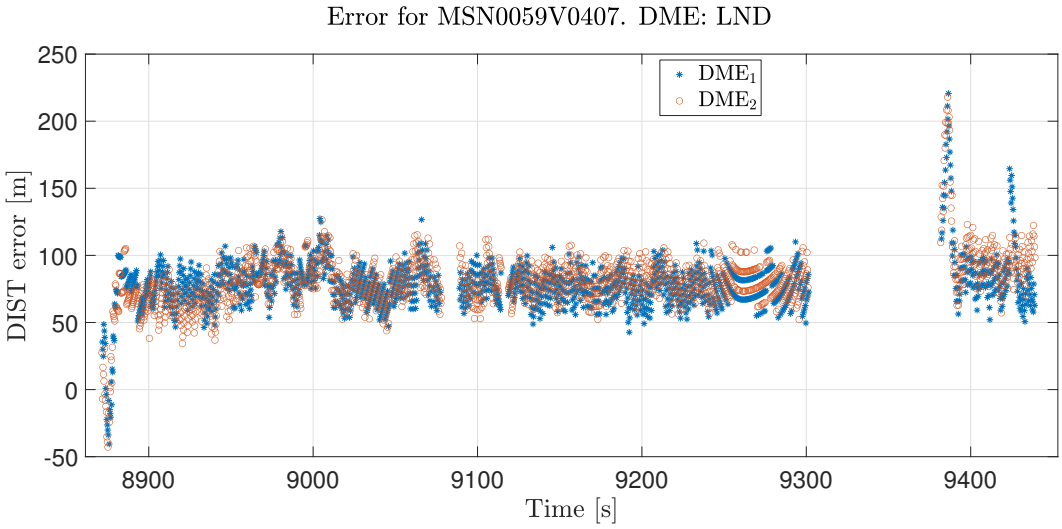

Fig. 3 Example of DME error signal for station LND.

For each DME station, the instantaneous error is obtained as the difference between the measured pseudorange and the theoretical range computed from the aircraft's GNSS-derived position using Equations 5–8. Measurements are grouped by station ID, producing discontinuous time series (Fig. 4). Segments are separated when time gaps exceed 10 s, and only segments with at least 100 samples are retained (Fig. 5), ensuring statistically homogeneous data for model identification.

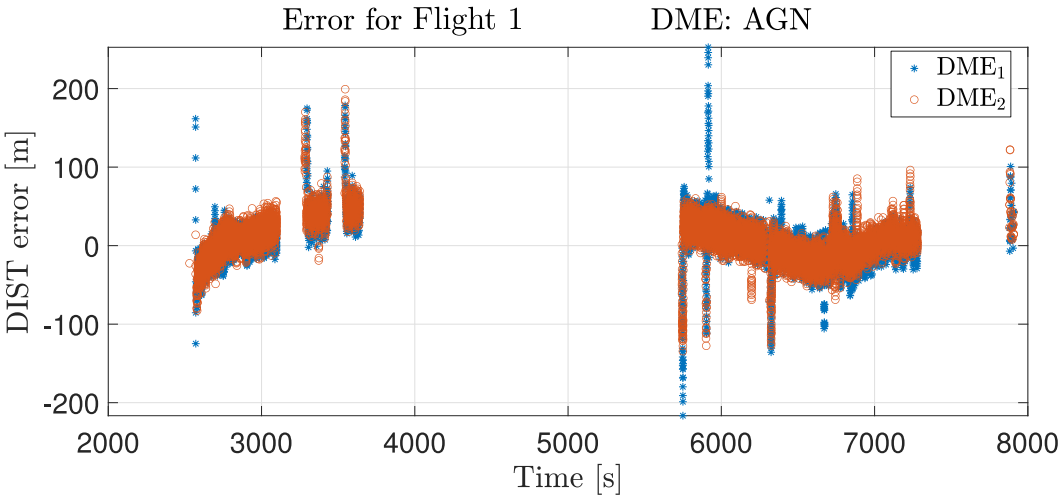

Fig. 4 Range error time series for DME station AGN (sides 1 and 2).

2.2.1 Mean Value Estimation

To separate the slowly varying bias from stochastic components and distinguish nominal noise from multipath errors, the mean offset $\bar{\varepsilon}(t)$ is estimated and removed. Three standard estimators are considered:

- **Arithmetic mean:**

$$\bar{\varepsilon} = \frac{1}{N_j} \sum_{i=1}^{N_j} \varepsilon(t_i), \tag{10}$$

where N_j is the number of samples in the segment.

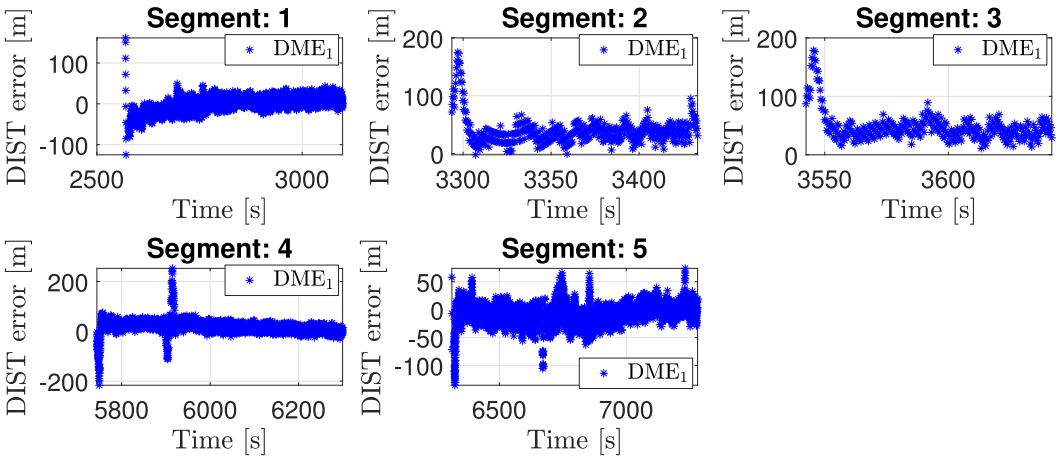

Fig. 5 Segmented range error signal for a single DME.

- **Moving average:**

$$\bar{\varepsilon}(t+1) = \bar{\varepsilon}(t) + \frac{1}{L}(\varepsilon(t+1) - \varepsilon(t-L+1)), \tag{11}$$

  where L is the window length.
- **Exponential moving average:**

$$\bar{\varepsilon}(t+1) = \alpha\bar{\varepsilon}(t) + (1-\alpha)\varepsilon(t+1), \tag{12}$$

  with $\alpha = 1 - e^{-\frac{\Delta t}{\tau}}$, where τ is the rise time and Δt the sampling interval.

A gated update mechanism mitigates the influence of outliers or multipath transients:

$$l_\varepsilon = \frac{(\varepsilon(t+1) - \bar{\varepsilon}(t))^2}{S_\varepsilon} \gtrless l_\alpha. \tag{13}$$

Assuming $r_\varepsilon = \varepsilon(t+1) - \bar{\varepsilon}(t) \sim \mathcal{N}(0, S_\varepsilon)$, l_α is computed via standard tables or $l_\alpha = \mathcal{F}^{-1}_{\chi^2}(1, P_{FA})$, with P_{FA} the false alarm probability. If $l_\varepsilon < l_\alpha$, α remains unchanged; otherwise, $\alpha = 1 - \exp^{-\frac{\Delta t}{k\tau}}$, where finite k yields a soft gate and $k \to \infty$ a hard gate. Filtering can be applied forward and backward to accommodate segments starting with large offsets. The optimal estimator $\bar{\varepsilon}_k(t)$ minimizes

$$k_j^* = \arg\min_k \left[(\mu_{\bar{\varepsilon}_k} - \mu_\varepsilon)^2 + \sigma^2(\bar{\varepsilon}_k)\right]. \tag{14}$$

2.2.2 Nominal and Multipath Separation

After mean removal, the residual innovation $\nu(t) = \varepsilon(t) - \bar{\varepsilon}(t)$ contains both nominal and multipath components. Separation is performed using the statistical test

$$\frac{\nu(t_i)^2}{S_0} \underset{Nominal}{\overset{Multipath}{\gtrless}} l_{MP}, \tag{15}$$

where S_0 is an initial variance estimate. This assumes multipath errors are rare and of limited amplitude, so the full-sample standard deviation approximates the nominal component. The threshold l_{MP} is chosen according to a target false-positive rate. Applying this test partitions the error signal into nominal errors $\{\varepsilon_{\text{Nom}}\}$ and multipath errors $\{\varepsilon_{\text{MP}}\}$. The subsets are refined iteratively using Algorithm 1.

Algorithm 1: Separation of nominal and multipath error

$S_i \leftarrow S_0$;
$\sigma_{Nom.,i} \leftarrow \sqrt{S_i}$;
while $|\sigma_{Nom.,i} - \sigma_{Nom.,i-1}| > \delta$ **do**
  $\{\varepsilon_{MP}\} = \{\varepsilon(t_i) \mid \frac{\nu(t_i)^2}{S_i} \geq l_{MP}\}$;
  $\{\varepsilon_{Nom.}\} = \{\varepsilon(t_i) \mid \frac{\nu(t_i)^2}{S_i} < l_{MP}\}$;
  $\sigma_{Nom.,i} \leftarrow \mathrm{std}(\varepsilon_{Nom.})$;
  $S_i \leftarrow \sigma^2_{Nom.,i}$;
end

The resulting subsets $\varepsilon_{n,k}$ and $\varepsilon_{mp,k}$ are used to identify the parameters of Eq. 9. Fig. 6 illustrates iterations of Algorithm 1 for real-flight data, which usually requires three iterations to converge. Once this division is obtained, the different parts of Eq. 9:

- $b_{DME}(t)$ is the quasi-constant offset of the nominal error, i.e. the mean value of $\varepsilon_{n,k}$.
- $b_{MP}(t)$ is the transient multipath error which is characterised by the amplitude (maximum and RMS) and duration of $\varepsilon_{mp,k}$. Naturally, only the parts of $\varepsilon_{mp,k}$ containing a significant number of points are regarded, to exclude misidentified samples (see Figure 6 at ~ 3590 s).
- $w(t)$ is the white Gaussian driving noise for the nominal error model, its variance is nominally given as the variance of $\varepsilon_{n,k}$.
- $h(t)$ is the linear filter that colours the driving noise, it is identified from $\varepsilon_{n,k}$ by frequency analysis.

can be identified. Fig. 6 illustrates iterative convergence, typically within three iterations.

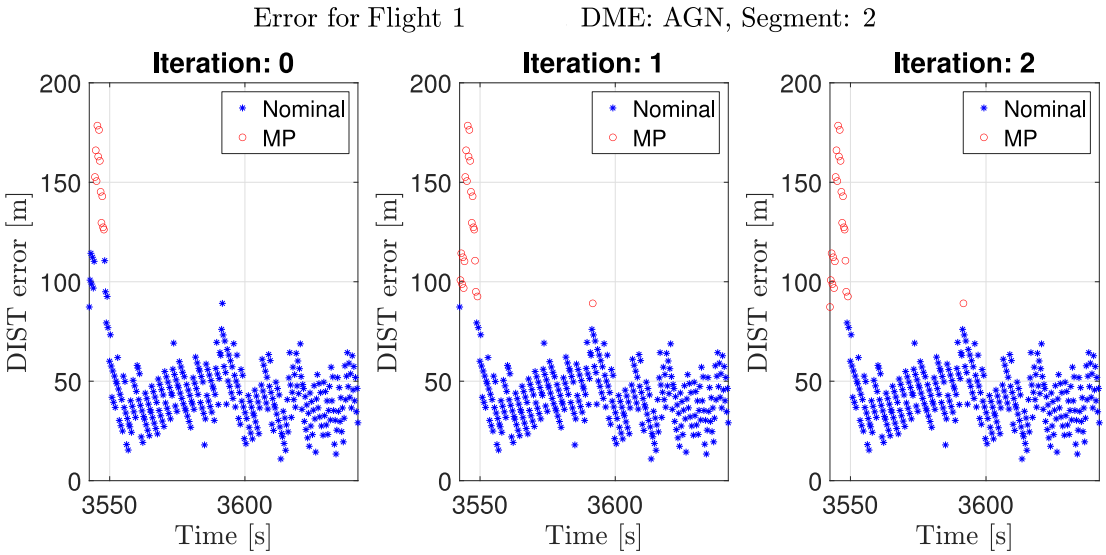

Fig. 6 Iterative classification of nominal and multipath errors for MSN0059V0393, AGN, segment 2.

2.2.3 Multipath and Nominal Noise Modeling

Multipath effects are modeled as transient offsets of finite duration:

$$b_{MP}(t) = \begin{cases} 0, & t < t_{MP} \\ \frac{b_{max}}{2}\left(1 - \cos\frac{2\pi t}{T}\right), & t_{MP} \le t \le t_{MP} + T \\ 0, & t > t_{MP} + T \end{cases} \tag{16}$$

where b_{max} and T are determined from flight data. The nominal stochastic component is modeled as filtered white Gaussian noise:

$$v_n(t) = \varepsilon_n(t) - \bar{\varepsilon}_n(t) = \int_0^t h(t-\tau)w(\tau)d\tau, \tag{17}$$

with $h(t)$ identified via a second-order autoregressive (AR) model:

$$H(z) = \frac{1}{1 - \sum_{k=1}^{2} a_k z^{-k}} \tag{18}$$

using the Burg method [31]. Example identification yields

$$H_{ex}(z) = \frac{1}{1 + 0.3168z^{-1} + 0.4154z^{-2}}, \tag{19}$$

indicating limited temporal correlation.

2.2.4 Nominal Bias Model

The slow bias b_{DME} is modeled as a random walk:

$$\dot{b}_{DME}(t) = n_b, \quad n_b \sim \mathcal{N}(0, W_{\dot{b}}), \quad b_{DME}(0) \sim \mathcal{N}(a\rho_{DME}, W_b), \tag{20}$$

where a captures weak range dependence:

$$\hat{a} = \frac{\sum_i \mu(\rho_{n,i})\mu(\varepsilon_{n,i})}{\sum_i \mu(\rho_{n,i})^2}. \tag{21}$$

The bias covariance is then

$$W_b = \left[\sigma(\boldsymbol{m}_{\varepsilon,seg} - \hat{a}\,\boldsymbol{m}_{\rho,seg})\right]^2. \tag{22}$$

2.2.5 Results and Identified Parameters

The model was identified using four representative flights (Fig. 7). Fig. 8 summarizes the measured quantities required to construct a representative DME model.

The nominal noise variance was found as $w(t) \sim \mathcal{N}(0, 182\,\mathrm{m}^2)$, with second-order shaping filter

$$H_{DME}(z) = \frac{1}{1 + 0.3684z^{-1} + 0.2739z^{-2}}. \tag{23}$$

Regression yielded $a = 1.2 \times 10^{-5}$ and process noise covariance $W_{\dot{b}} = 6.25\,\mathrm{m}^2/\mathrm{s}$. Multipath amplitudes and durations follow inverse Gaussian distributions ($\mu_{amp} = 12$, $\Lambda_{amp} = 6$; $\mu_{dur} = 1.3$, $\Lambda_{dur} = 124$) and are typically shorter than 30 s, enabling robust fault detection in fusion filters.

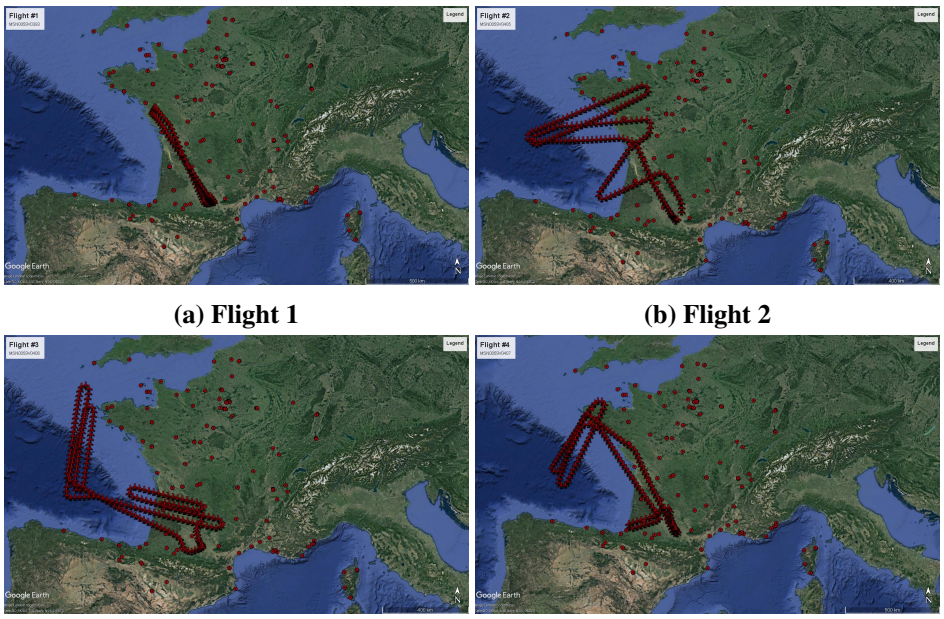

(a) Flight 1 **(b) Flight 2**

(c) Flight 3 **(d) Flight 4**

Fig. 7 Flights used to construct the DME error model.

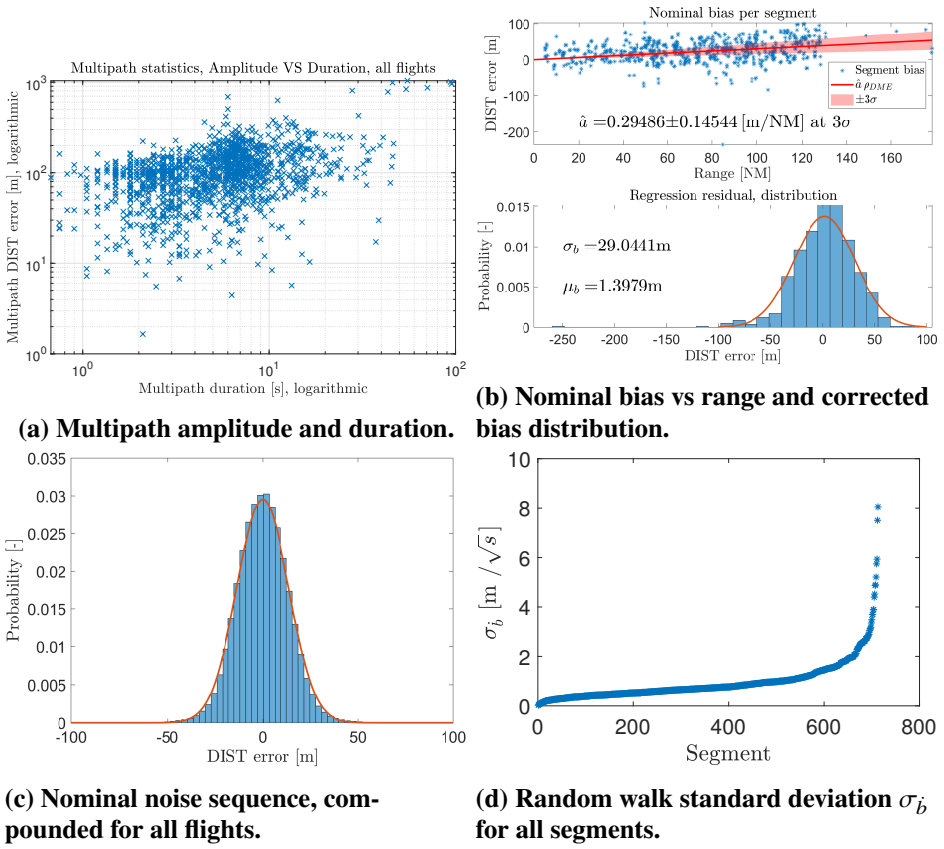

(a) Multipath amplitude and duration.

(b) Nominal bias vs range and corrected bias distribution.

(c) Nominal noise sequence, compounded for all flights.

(d) Random walk standard deviation $\sigma_{\dot{b}}$ for all segments.

Fig. 8 Summary of real-flight data measurements for DME model identification.

The identified parameters $b_{DME}(t)$, $b_{MP}(t)$, and $h(t)$ form the basis for defining adaptive measurement covariances in the hybrid navigation filter (Section 3).

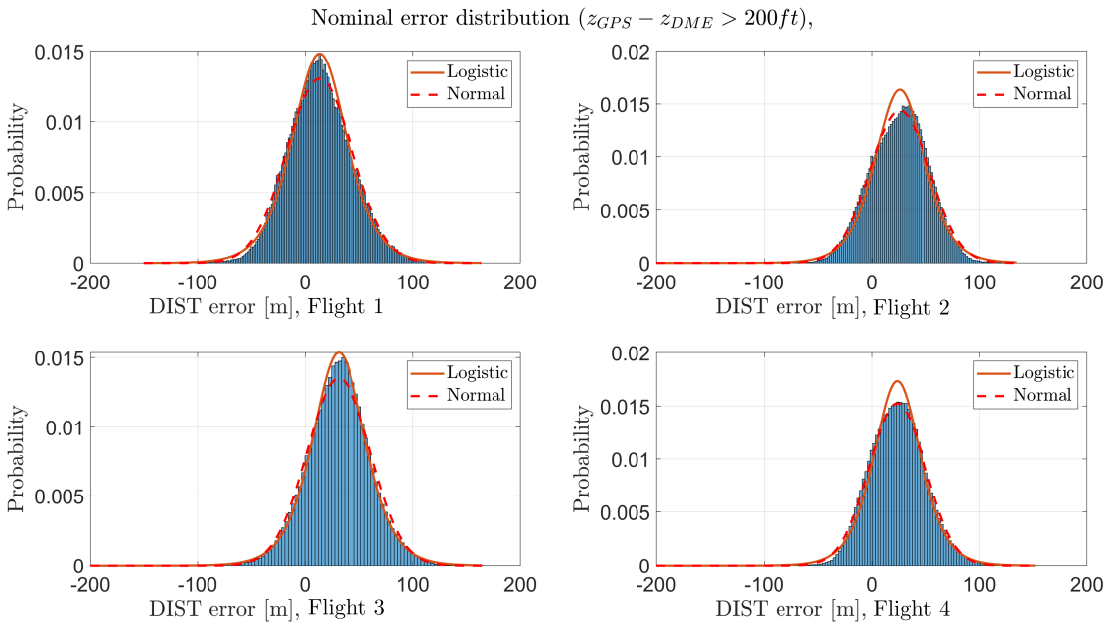

Fig. 9 Nominal error distribution after mean and multipath separation.

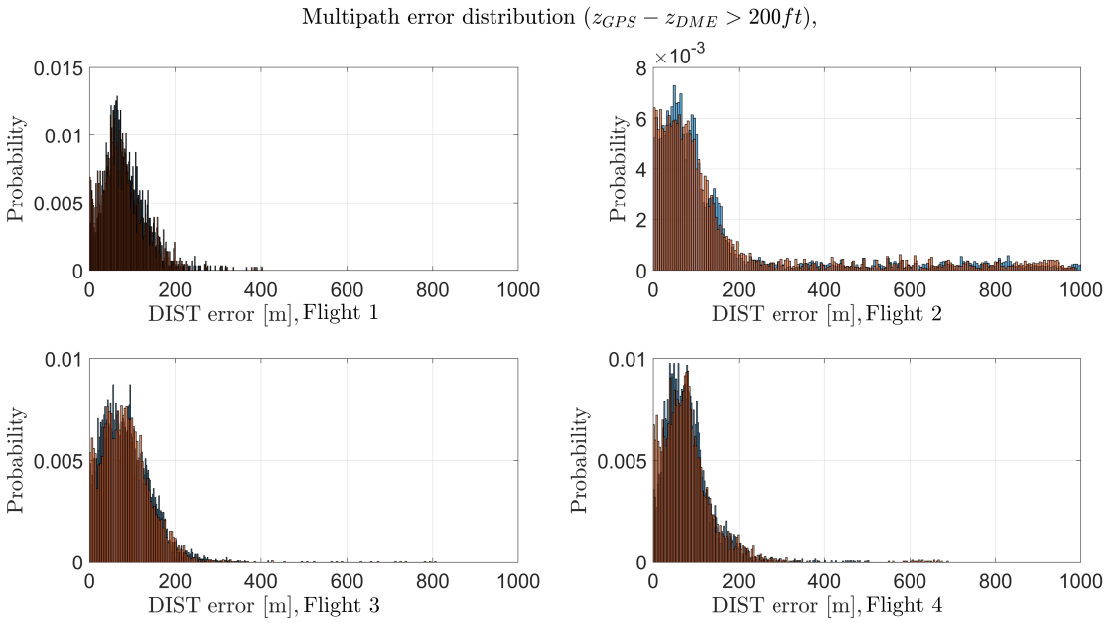

Fig. 10 Multipath error distribution.

3 Integration of DME measurements in a Multisensor Data Navigation Filter

This section discusses the integration of DME observations into a navigation filter that already incorporates visual measurements [24]. Besides GNSS/IRS data, the filter uses visual information from a cockpit-mounted monocular camera. Specifically, the pixel coordinates of the four runway corners are

extracted using a YOLOV11 model [24]. Relying solely on visual data has limitations: the filter needs GNSS/IRS initialization, camera resolution restricts reliable measurements to short range (final approach), and poor visual conditions (e.g., clouds) may degrade accuracy or temporarily prevent measurements.

3.1 Navigation Filter Mechanics and Uncertainty Representation

The navigation filter in the MDF is an extended Kalman filter [32], which approximates nonlinear uncertainty propagation [5]. The continuous-time dynamics of the system can be written as

$$\mathcal{M}(t) : \begin{cases} \vec{x}(t) = f(\vec{x}(t), \vec{u}(t), \vec{v}(t)) \\ \vec{y}(t) = h(\vec{x}(t), \vec{w}(t)) \end{cases} \tag{24}$$

where $\vec{x}$ is the state, $\vec{u}$ the input, $\vec{y}$ the measurement vector, and $\vec{v}$, $\vec{w}$ are Gaussian noises with covariances $V(t)$ and $W(t)$. For filter implementation, a discrete-time model is used:

$$\mathcal{M}_d(t_k) : \begin{cases} \vec{x}_{t_{k+1}} = f_d(\vec{x}_{t_k}, \vec{u}_{t_k}, \vec{v}_{t_k}) \\ \vec{y}_{t_{k+1}} = h(\vec{x}_{t_{k+1}}, \vec{w}_{t_{k+1}}) \end{cases} \tag{25}$$

The continuous-to-discrete conversion is done via forward Euler integration. Linearisation about the current state and input gives:

$$\begin{aligned} \vec{x}_{t_{k+1}} &= F_{t_k}\vec{x}_{t_k} + G_{u,t_k}\vec{u}_{t_k} + G_{v,t_k}\vec{v}_{t_k} \\ \vec{y}_{t_{k+1}} &= H_{t_{k+1}}\vec{x}_{t_{k+1}} + H_{w,t_{k+1}}\vec{w}_{t_{k+1}} \end{aligned} \tag{26}$$

where the Jacobians are defined as

$$\begin{aligned} F_{t_k} &= \left.\frac{\partial f_d}{\partial \vec{x}}\right|_{\vec{x}_{t_k},\vec{u}_{t_k}}, \quad G_{u,t_k} = \left.\frac{\partial f_d}{\partial \vec{u}}\right|_{\vec{x}_{t_k},\vec{u}_{t_k}}, \quad G_{v,t_k} = \left.\frac{\partial f_d}{\partial \vec{v}}\right|_{\vec{x}_{t_k},\vec{u}_{t_k}} \\ H_{t_k} &= \left.\frac{\partial h}{\partial \vec{x}}\right|_{\vec{x}_{t_k}}, \qquad H_{w,t_k} = \left.\frac{\partial h}{\partial \vec{w}}\right|_{\vec{x}_{t_k}} \end{aligned} \tag{27}$$

The state estimate $\hat{\vec{x}}$ and its covariance P are computed through a prediction-correction cycle. The prediction step is:

$$\begin{aligned} \hat{\vec{x}}_{t_{k+1}|t_k} &= f(\vec{x}_{t_k}, \vec{u}_{t_k}, 0) \\ P_{t_{k+1}|t_k} &= F_{t_k}P_{t_k}F_{t_k}^T + G_{v,t_k}V_{t_k}G_{v,t_k}^T \end{aligned} \tag{28}$$

The innovation step computes the measurement residual:

$$\begin{aligned} \vec{\nu}_{t_{k+1}} &= \vec{y}_{t_{k+1}} - h(\hat{\vec{x}}_{t_{k+1}|t_k}, 0) \\ S_{t_{k+1}} &= H_{t_{k+1}}P_{t_{k+1}|t_k}H_{t_{k+1}}^T + H_{w,t_{k+1}}W_{t_{k+1}}H_{w,t_{k+1}}^T \end{aligned} \tag{29}$$

The correction step updates the state and covariance:

$$\begin{aligned} K_{t_{k+1}} &= P_{t_{k+1}|t_k}H_{t_{k+1}}^T S_{t_{k+1}}^{-1} \\ \hat{\vec{x}}_{t_{k+1}} &= \hat{\vec{x}}_{t_{k+1}|t_k} + K_{t_{k+1}}\vec{\nu}_{t_{k+1}} \\ P_{t_{k+1}} &= (I - K_{t_{k+1}}H_{t_{k+1}})P_{t_{k+1}|t_k}(I - K_{t_{k+1}}H_{t_{k+1}})^T + K_{t_{k+1}}H_{w,t_{k+1}}W_{t_{k+1}}H_{w,t_{k+1}}^T K_{t_{k+1}}^T \end{aligned} \tag{30}$$

Uncertainties are represented by covariance matrices Σ, which define ellipsoids in the corresponding reference frame. For a position estimate $\hat{\vec{\xi}}_E$ in the E-frame, the error $\vec{\varepsilon}_\xi = \vec{\xi}_E - \hat{\vec{\xi}}_E$ is described by:

$$\vec{\delta}_E^T \Sigma_{\xi_E}^{-1} \vec{\delta}_E \leq 1 \tag{31}$$

The ellipsoid axes are given by the eigenvalues and eigenvectors of Σ_{ξ_E}. For an arbitrary direction $\vec{e}_N$ in the N-frame, the variance is obtained as

$$r = \sqrt{\frac{1}{\vec{e}_E^T \Sigma_{\xi_E}^{-1} \vec{e}_E}}, \quad \vec{e}_E = R_{E,N} \vec{e}_N \tag{32}$$

Alternatively, the covariance can be transformed to another frame:

$$\Sigma_{\xi_N} = (R_{N,E} \Sigma_{\xi_E}^{-1} R_{E,N})^{-1} \tag{33}$$

This matrix is used, for example, to compute protection levels in the N-frame.

3.2 Loose-Coupled MDF Algorithm

A loose-coupled navigation filter is designed to integrate DME measurements into the aircraft state estimation. The state vector consists of position and velocity in the E-frame and accelerometer bias in the B-frame:

$$\vec{X} = \begin{pmatrix} \vec{P}_E \\ \vec{V}_E \\ \vec{B}_{A,B} \end{pmatrix}. \tag{34}$$

The filter inputs are B-frame accelerations $\vec{A}_B$ and Euler angles $\vec{\vartheta} = (\varphi, \theta, \psi)^T$. The transformation B→E is found in Section 2.1. Supposedly known model parameters include the local gravity vector $\vec{g}$ and Earth's rotation rate $\vec{\omega}_T$. The state dynamics in the E-frame, with a random walk model for the accelerometer bias, are:

$$\dot{\vec{X}} = \begin{pmatrix} \dot{\vec{P}}_E \\ \dot{\vec{V}}_E \\ \dot{\vec{B}}_{A,B} \end{pmatrix} = \begin{pmatrix} \vec{V}_E \\ \dot{\vec{V}}_E \\ \vec{v}_{B_{A,B}} \end{pmatrix}, \tag{35}$$

where $\vec{v}_{B_{A,B}}$ is the process noise driving the bias. Body-mounted accelerometers measure the aircraft acceleration:

$$\vec{A}_{B,m} = R_{B,N} R_{N,E} \dot{\vec{V}}_E + R_{B,N} \vec{g} + 2 R_{B,N} R_{N,E} (\vec{V}_E \times \vec{\omega}_T) + \vec{B}_{A,B} + \vec{v}_{A,B}, \tag{36}$$

where $\vec{v}_{A,B}$ is accelerometer noise and $\vec{g} = g\vec{e}_3$ is the normal gravity.

Solving for $\dot{\vec{V}}_E$ gives:

$$\dot{\vec{V}}_E = R_{E,N} R_{N,B} \vec{A}_{B,m} - R_{E,N} \vec{g} - 2(\vec{V}_E \times \vec{\omega}_T) - R_{E,N} R_{N,B} (\vec{B}_{A,B} + \vec{v}_{A,B}). \tag{37}$$

Instead of direct acceleration, the measured load factor $n_{B,m} = \vec{A}_{B,m}/g$ can be used. Then the velocity dynamics become:

$$\dot{\vec{V}}_E = R_{E,N} \left[\vec{e}_3 + R_{N,B} (\vec{n}_{B,m} - \vec{B}_{n,B} + \vec{v}_{n,B}) \right] g + 2(\vec{\omega}_T)_\times \vec{V}_E. \tag{38}$$

Finally, the complete state dynamics are:

$$\dot{\vec{X}} = \begin{pmatrix} \dot{\vec{P}}_E \\ \dot{\vec{V}}_E \\ \dot{\vec{B}}_{A,B} \end{pmatrix} = \begin{pmatrix} \vec{V}_E \\ R_{E,N} \left[\vec{e}_3 + R_{N,B} (\vec{n}_{B,m} - \vec{B}_{n,B} + \vec{v}_{n,B}) \right] g + 2(\vec{\omega}_T)_\times \vec{V}_E \\ \vec{v}_{A,B} \end{pmatrix}. \tag{39}$$

3.2.1 Measurement Models

The loose-coupled filter uses ranges from two DME receivers ($\rho_{DME,1}, \rho_{DME,2}$), and pressure altitude (z_p). It also uses visual measurements for the landing phase consisting of the four runway corners using YOLOv11 (detailed in [24]).

DME measurements:
The ideal range to the DME ith station is

$$\rho_{A/C,DME_i} = \left\| \vec{P}_E - \vec{P}_{DME,i} \right\|. \tag{40}$$

With Gaussian noise and optional quasi-constant bias:

$$\begin{pmatrix} \rho_{DME_1,m} \\ \rho_{DME_2,m} \end{pmatrix} = \begin{pmatrix} \left\| \vec{P}_E - \vec{P}_{DME_1} \right\| + b_{DME_1} + w_{DME_1} \\ \left\| \vec{P}_E - \vec{P}_{DME_2} \right\| + b_{DME_2} + w_{DME_2} \end{pmatrix}. \tag{41}$$

However, estimating these biases requires the simultaneous availability of both GNSS and DME measurements, which cannot be guaranteed within the scope of this solution.

Since DME stations are often low-elevation relative to the aircraft, vertical observability is low. Since the vertical channel is in the non-GNSS case ensured by the barometric altitude it is used to eliminate the impact of the DME measurement in this estimated direction. The DME distance which is used for correcting the horizontal position is thus the length of the DME to aircraft vector projected unto the local horizontal plane, i.e. perpendicular to gravity. Denoting the DME distance vector (aircraft to DME i) by $\vec{D}_{A/C,DME_i,E} \triangleq \vec{P}_E - \vec{P}_{DME,i}$, in the N-frame we have $\vec{D}_{A/C,DME_i,N} = R_{E,N}\vec{D}_{A/C,DME_i,E}$, the vertical component can be removed using

$$\vec{D}_{A/C,DME_i,E,\perp} = R_{N,E}\Big[T\left(R_{E,N}\vec{D}_{A/C,DME_i,E}\right)\Big], \quad T = \begin{pmatrix} 1 & 0 & 0 \\ 0 & 1 & 0 \\ 0 & 0 & 0 \end{pmatrix}. \tag{42}$$

The corresponding horizontal distance measurement is

$$\rho_{DME_i,m,\perp} = \rho_{DME_i,m} \left\| T\, \vec{e}_{A/C,DME_i,N} \right\|. \tag{43}$$

This yields the pseudo-measurement:

$$\begin{aligned} \nu_{DME_i} &\triangleq -\big(\rho_{DME_i,m,\perp} - \|\vec{D}_{A/C,DME_i,E,\perp}\|\big) \\ &\approx -\big(\rho_{DME_i,m} - \|\vec{D}_{A/C,DME_i,E,\perp}\|\big) - \|T\,\vec{e}_{A/C,DME_i,N}\|\, w_{DME_i}. \end{aligned} \tag{44}$$

Pressure altitude:
Pressure altitude z_p expressed as a geoid height is derived from $\vec{P}_E$ via geodetic latitude, using, e.g., the method of [30]. The altitude in the E-frame is

$$z = \|\vec{P}_E - \vec{P}_{E,0}\|, \tag{45}$$

with $\vec{P}_{E,0}$ obtained from $(\lambda, \phi, h) \to (\lambda, \phi, 0)$. The measurement model is then

$$z_p = \|\vec{P}_E - \vec{P}_{E,0}\| + w_{z_p}. \tag{46}$$

Vision measurements:
The AI-based vision algorithm detects and identifies the runway corners in the image plane. The measurement is given as coordinates in the image plane for each identified corner A_i:

$$\vec{y}_{vision_i} = \begin{bmatrix} u_i \\ v_i \end{bmatrix} = \begin{bmatrix} f_x \frac{y_C^{A_i}}{x_C^{A_i}} + c_x + w_{u_i} \\ f_y \frac{z_C^{A_i}}{x_C^{A_i}} + c_y + w_{v_i} \end{bmatrix} = h_{vision_i}(\vec{x}, \vec{w}_{vision_i}) \tag{47}$$

where $f_{x/y/z}$ are camera focal lengths and $(x, y, z)_C^{A_i}$ is the vector from the camera origin to the runway corner A_i, expressed in the camera frame. Details are found in [24]. The $N \in [0, 4]$ detected corners concatenate to the measurement vector $\vec{y}_{vision}$ and the corresponding measurement equations h_{vision}

$$\vec{y}_{vision} = \begin{pmatrix} \vec{y}_{vision_1} \\ \vdots \\ \vec{y}_{vision_N} \end{pmatrix}, \quad h_{vision}(\vec{x}, \vec{w}) = \begin{pmatrix} h_{vision_1}(\vec{x}, \vec{w}_{vision_1}) \\ \vdots \\ h_{vision_N}(\vec{x}, \vec{w}_{vision_N}) \end{pmatrix}$$

The Jacobian of the measurement is $H_{vision} = \frac{\partial h_{vision}}{\partial \vec{x}}$ is also found in [24].

3.2.2 Filter Synthesis

The navigation filter can be summarized as follows. The state, input, and process noise vectors are

$$\vec{x} = \begin{pmatrix} \vec{P}_E \\ \vec{V}_E \\ \vec{B}_{n,B} \end{pmatrix}, \quad \vec{u} = \begin{pmatrix} \vec{n}_{B,m} \\ \varphi \\ \theta \\ \psi \end{pmatrix}, \quad \vec{v} = \begin{pmatrix} \vec{v}_n \\ \vec{v}_{B_n} \\ v_\varphi \\ v_\theta \\ v_\psi \end{pmatrix}. \tag{48}$$

The dynamics are

$$\dot{\vec{x}} = \begin{pmatrix} \vec{V}_E \\ R_{E,N}\left[\vec{e}_3 + R_{N,B}(\vec{n}_{B,m} - \vec{B}_{n,B} + \vec{v}_{n,B})\right] g + 2(\vec{\omega}_T)_\times \vec{V}_E \\ \vec{n}_{A,B} \end{pmatrix} := f(\vec{x}, \vec{u}, \vec{v}). \tag{49}$$

The measurement and measurement noise vectors are

$$\vec{y} = \begin{pmatrix} \nu_{DME_1} \\ \nu_{DME_2} \\ z_p \\ \vec{y}_{vision} \end{pmatrix}, \quad \vec{w} = \begin{pmatrix} \vec{w}_{DME_1} \\ \vec{w}_{DME_2} \\ w_{z_p} \\ \vec{w}_{vision} \end{pmatrix}. \tag{50}$$

Yielding the measurement model

$$\vec{y} = \begin{pmatrix} \nu_{DME_1} \\ \nu_{DME_2} \\ z_p \\ \vec{y}_{vision} \end{pmatrix} = \underbrace{\begin{pmatrix} -\left(\rho_{DME_1,m}||T\,\vec{e}_{A/C,DME_1,N}|| - ||\vec{D}_{A/C,DME_1,E,\perp}||\right) + ||T\,\vec{e}_{A/C,DME_1,N}||\,w_{DME_1} \\ -\left(\rho_{DME_2,m}||T\,\vec{e}_{A/C,DME_2,N}|| - ||\vec{D}_{A/C,DME_2,E,\perp}||\right) + ||T\,\vec{e}_{A/C,DME_2,N}||\,w_{DME_2} \\ ||\vec{P}_E - \vec{P}_{E,0}|| + w_{z_p} \\ \vec{h}_{vision}(\vec{x}, \vec{w}_{vision}) \end{pmatrix}}_{h(\vec{x},\vec{w})} \tag{51}$$

State Jacobian:

Linearizing the state dynamics, the symbolic matrix is given by

$$F(\vec{x}, \vec{u}, \vec{v}) = \begin{pmatrix} \mathbf{0} & I & \mathbf{0} \\ \dfrac{\partial\left[R_{E,N}R_{N,B}\left(\vec{A}_{B,m} - \vec{B}_{A,B} - \vec{n}_A\right)\right]}{\partial \vec{P}_E} & 2\,(\vec{\omega}_T)_\times & -R_{E,N}R_{N,B} \\ \mathbf{0} & \mathbf{0} & \mathbf{0} \end{pmatrix} \tag{52}$$

The partial derivative in the first column of the second row is difficult to express explicitly, owing to the highly nonlinear dependence of $R_{E,N}$ on the geodetic latitude ϕ, longitude λ, and the E-frame position $\vec{P}_E$. However, the angular errors associated with the Euler angles of $R_{N,B}$ dominate those induced by $R_{E,N}$, even for position errors on the order of ∼1 NM, except at very high latitudes. Consequently, it is reasonable to neglect the dependence of $R_{E,N}$ on $\vec{P}_E$ and treat it as a constant during linearization. Under this assumption, the system matrix simplifies to

$$F(\vec{x}, \vec{u}, \vec{v}) = \begin{pmatrix} \mathbf{0} & I & \mathbf{0} \\ \mathbf{0} & (\vec{\omega}_T)_\times & -R_{E,N}R_{N,B} \\ \mathbf{0} & \mathbf{0} & \mathbf{0} \end{pmatrix}. \tag{53}$$

Noise Jacobian:

Accounting for input uncertainties yields

$$G_v(\vec{x}, \vec{u}, \vec{v}) = \begin{pmatrix} \mathbf{0} & \mathbf{0} & \mathbf{0} \\ -R_{E,N}R_{N,B} & \mathbf{0} & g\,R_{E,N}\frac{\partial R_{N,B}(\vec{n}_{B,m} - \vec{B}_{n,B})}{\partial \vartheta} \\ \mathbf{0} & I & \mathbf{0} \end{pmatrix}. \tag{54}$$

The partial derivative of the rotation term is

$$\frac{\partial R_{N,B}(\vec{n}_{B,m} - \vec{B}_{n,B} + \vec{v}_{n,B})}{\partial \vartheta} \triangleq \begin{pmatrix} \Delta_{1,1} & \Delta_{1,2} & \Delta_{1,3} \\ \Delta_{2,1} & \Delta_{2,2} & \Delta_{2,3} \\ \Delta_{3,1} & \Delta_{3,2} & \Delta_{3,3} \end{pmatrix}, \tag{55}$$

where the individual elements are

$$
\begin{aligned}
\Delta_{1,1} &= v_2(\mathrm{s}_\varphi \mathrm{s}_\psi + \mathrm{c}_\varphi \mathrm{c}_\psi \mathrm{s}_\theta) + v_3(\mathrm{c}_\varphi \mathrm{s}_\psi - \mathrm{c}_\psi \mathrm{s}_\varphi \mathrm{s}_\theta) \\
\Delta_{1,2} &= v_3 \mathrm{c}_\varphi \mathrm{c}_\psi \mathrm{c}_\theta - v_1 \mathrm{c}_\psi \mathrm{s}_\theta + v_2 \mathrm{c}_\psi \mathrm{c}_\theta \mathrm{s}_\varphi \\
\Delta_{1,3} &= v_3(\mathrm{c}_\psi \mathrm{s}_\varphi - \mathrm{c}_\varphi \mathrm{s}_\psi \mathrm{s}_\theta) - v_2(\mathrm{c}_\varphi \mathrm{c}_\psi + \mathrm{s}_\varphi \mathrm{s}_\psi \mathrm{s}_\theta) - v_1 \mathrm{c}_\theta \mathrm{s}_\psi \\
\Delta_{2,1} &= -v_2(\mathrm{c}_\psi \mathrm{s}_\varphi - \mathrm{c}_\varphi \mathrm{s}_\psi \mathrm{s}_\theta) - v_3(\mathrm{c}_\varphi \mathrm{c}_\psi + \mathrm{s}_\varphi \mathrm{s}_\psi \mathrm{s}_\theta) \\
\Delta_{2,2} &= v_3 \mathrm{c}_\varphi \mathrm{c}_\theta \mathrm{s}_\psi - v_1 \mathrm{s}_\psi \mathrm{s}_\theta + v_2 \mathrm{c}_\theta \mathrm{s}_\varphi \mathrm{s}_\psi \\
\Delta_{2,3} &= v_3(\mathrm{s}_\varphi \mathrm{s}_\psi + \mathrm{c}_\varphi \mathrm{c}_\psi \mathrm{s}_\theta) - v_2(\mathrm{c}_\varphi \mathrm{s}_\psi - \mathrm{c}_\psi \mathrm{s}_\varphi \mathrm{s}_\theta) + v_1 \mathrm{c}_\psi \mathrm{c}_\theta \\
\Delta_{3,1} &= v_2 \mathrm{c}_\varphi \mathrm{c}_\theta - v_3 \mathrm{c}_\theta \mathrm{s}_\varphi \\
\Delta_{3,2} &= -v_1 \mathrm{c}_\theta - v_3 \mathrm{c}_\varphi \mathrm{s}_\theta - v_2 \mathrm{s}_\varphi \mathrm{s}_\theta \\
\Delta_{3,3} &= 0
\end{aligned}
\tag{56}
$$

with elements defined in terms of $v = \vec{n}_{B,m} - \vec{B}_{n,B}$ and the shorthand $\mathrm{s}_* = \sin(*), \mathrm{c}_* = \cos(*)$.

Measurement Jacobian:

For horizontally decoupled DME:

$$
H(\vec{x}, \vec{w}) = \begin{pmatrix}
R_{E,N} \frac{T R_{E,N}^T (\vec{P}_E - \vec{P}_{DME_1})/\|\vec{P}_E - \vec{P}_{DME_1}\|}{\|T R_{E,N}^T (\vec{P}_E - \vec{P}_{DME_1})/\|\vec{P}_E - \vec{P}_{DME_1}\|\|} & \mathbf{0} & \mathbf{0} \\
R_{E,N} \frac{T R_{E,N}^T (\vec{P}_E - \vec{P}_{DME_2})/\|\vec{P}_E - \vec{P}_{DME_2}\|}{\|T R_{E,N}^T (\vec{P}_E - \vec{P}_{DME_2})/\|\vec{P}_E - \vec{P}_{DME_2}\|\|} & \mathbf{0} & \mathbf{0} \\
\frac{\vec{P}_E - \vec{P}_{E,0}}{\|\vec{P}_E - \vec{P}_{E,0}\|} & \mathbf{0} & \mathbf{0} \\
H_{vision} & \mathbf{0} & \mathbf{0}
\end{pmatrix}.
\tag{57}
$$

The E-frame correction directions are given by the unit vectors (or projected) between the estimated aircraft position and the reference points, showing that DME geometry strongly affects position estimation without GNSS.

3.2.3 Filter Tuning

Filter tuning involves specifying the process and measurement noise covariance matrices, V_{t_k} and $W_{t_{k+1}}$. Here, both can be assumed diagonal:

$$
V_{t_k} = \mathrm{diag}(\sigma^2_{A_{B,x}}, \sigma^2_{A_{B,y}}, \sigma^2_{A_{B,z}}, \sigma^2_{B_{A,B,x}}, \sigma^2_{B_{A,B,y}}, \sigma^2_{B_{A,B,z}}),
\tag{58}
$$

$$
W_{t_{k+1}} = \mathrm{diag}(\sigma^2_{\rho_{DME_1}}, \sigma^2_{\rho_{DME_2}}, \sigma^2_{z_p}, \sigma^2_{y_{vision}}).
\tag{59}
$$

Standard deviations are taken from sensor specs, experiments, or error models. Acceleration terms are set from experimental data; accelerometer bias random walk is taken from sensor specifications. DME noise $\sigma_{\rho_{DME_j}}$ includes bias and transients, approximated in the EKF as white noise to prioritize robustness, the vision related term is found through experimental data.

Adaptive noise tuning (covariance bloating)

To mitigate DME transients, a simple variance adapter inflates the measurement covariance based on the Kalman innovation. In the scalar case (Fig. 11), if the predicted and measured covariance ellipsoids do not intersect, the measurement covariance is "bloated" to ensure consistency.

For a probability level of n_σ standard deviations, the inflated innovation covariance is

$$
S_\gamma = \frac{\vec{\gamma}\,\vec{\gamma}^T}{n_\sigma^2}.
\tag{60}
$$

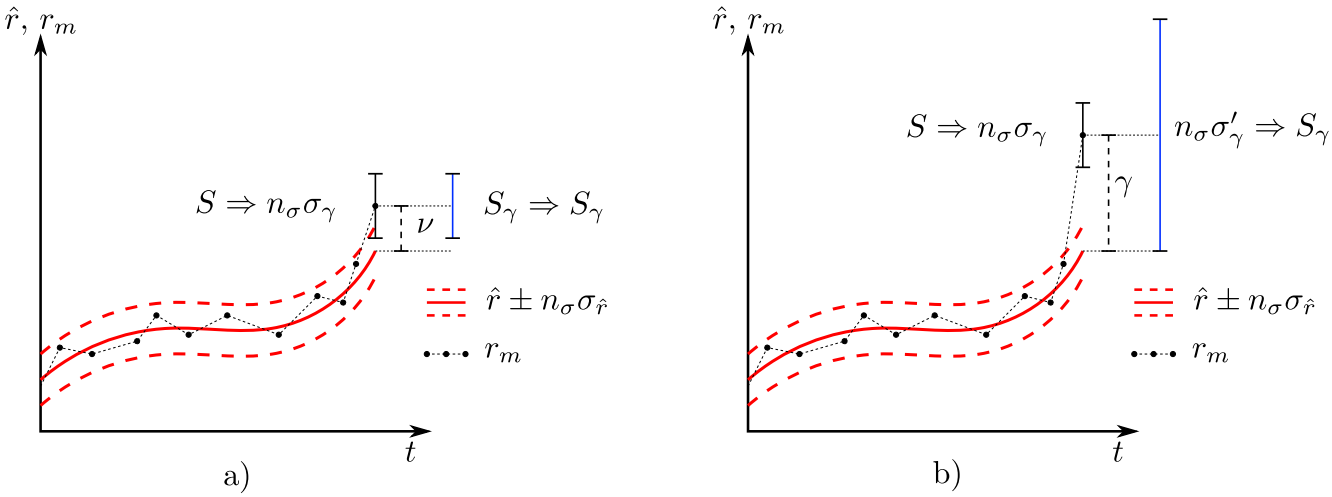

Fig. 11 Outlier mitigation through covariance bloating in the scalar case: a) Nominal case with uncertainty intersection; b) Covariance bloating when no intersection.

This bloated S_γ is used to compute the Kalman gain.

4 Hybrid PBVS Approach and Landing Strategy

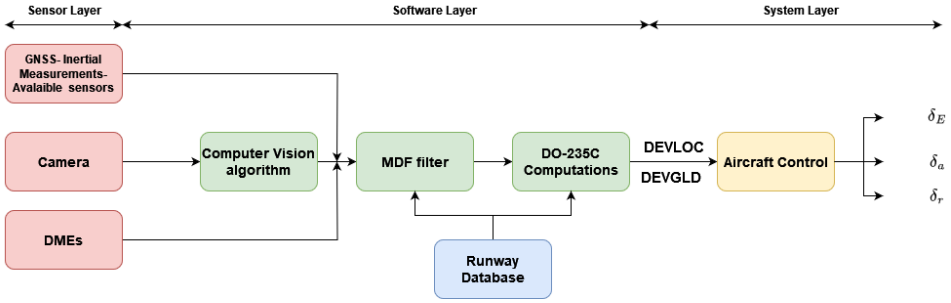

Fig. 12 General block diagram of the PBVS software solution [32].

The proposed control strategy, shown in Fig. 12 and detailed in [24, 32], decouples aircraft pose estimation from control law computation. The sensor layer gathers DME, IRS, Visual, and ADR data. The software layer executes the navigation filter and computes ILS-like lateral and longitudinal control deviations, respectively DEVLOC and DEVGLD, while the system layer applies the corresponding control laws.

4.1 Implementation

The guidance and control strategy is validated using a high-fidelity real-time simulation platform developed at ONERA [25]. The software/hardware setup ensures tight coupling between flight dynamics and the visual environment, allowing state observation, computer vision processing, virtual sensor fusion, and full aircraft control. A Boeing 747 model is used as the simulated aircraft. The simulator generates a synthetic video stream with Microsoft Flight Simulator 2020 (MSFS) on one computing unit, coupled to a Speedgoat real-time machine providing aircraft pose. A second unit processes the video for runway detection [24], while a third executes the MDF layer. The control strategy is tested through multiple autonomous flights starting sufficiently far from the destination runway to capture several DME signals.

During en-route and approach phases, attitude control with heading tracking is maintained. At 10 km from the runway, the system switches to capturing and tracking localizer and glide deviations [24, 32].

Fig. 13 Visualization of different landings on the LFBO 32L and 32R runways.

To emphasize DME usage, multiple landings at Toulouse Airport (LFBO) are conducted using four real and artificial DME stations. IRS and AI-based measurements also feed the MDF filter. Scenarios include lost or inaccurate visual measurements due to false detections from the parallel runway, as illustrated in Fig. 13.

4.2 Results of Multiple Autonomous Landings

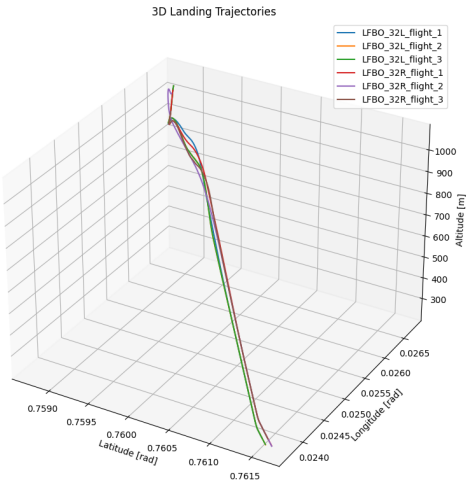

Fig. 14 3D trajectories of landings on LFBO 32L and 32R runways.

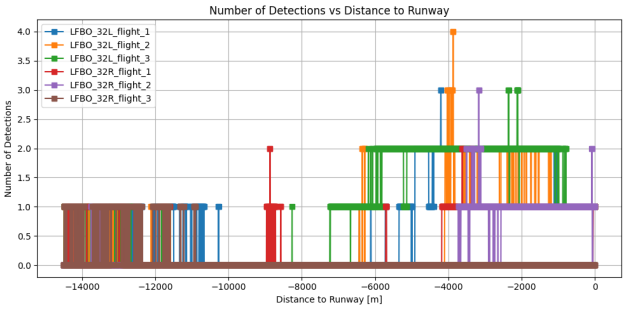

Fig. 15 Number of runways detected as a function of distance to the runway of interest.

All flights start from 15 km away to the runway, at λ =1.5319 °, ϕ =43.4723 °, Z =3400 ft, with initial attitude ψ =-62 °, θ =-3 °, φ=2.5 °, velocity 240 kts, and angular rates $\dot{\psi}$ =-0.3 °/s, $\dot{\theta}$=-1.12 °/s, $\dot{\varphi}$=0 °/s. Various weather and lighting conditions are considered, highlighting the sensitivity of vision-based control [24, 25, 32]. Among the six autonomous landings performed on the real-time simulation platform, shown in Fig. 13 and Fig. 14, comparable performance levels were achieved across all trials.

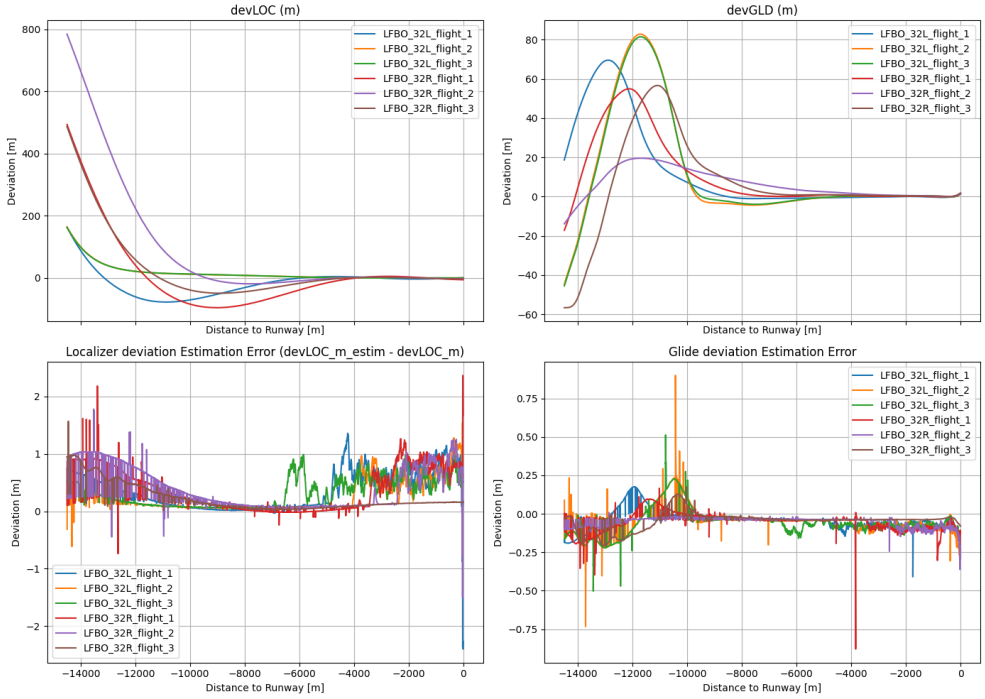

Fig. 16 Estimated localizer (DEVLOC) and glide (DEVGLD) deviations (top) and corresponding errors (bottom) versus distance to the runway, for autonomous landings on LFBO 32L and 32R with visual conditions from Fig. 13.

As illustrated in Fig. 15 and Fig. 13, a significant number of false detections occur during the early stages of the approach. These false detections are mainly due to the identification of a runway different from the intended one. For instance, during the LFBO_32L_flight_1 landing on the 32L runway (left snapshots in Fig. 13), the YOLOV11 model occasionally detects the parallel 32R runway with a sufficiently high confidence score, leading to its inclusion in the MDF filter as if it were the target runway 32L. As seen in Fig. 15, such misdetections are recurrent across all approaches: between 15 km and 6 km from the runway threshold, the model often fails to identify the correct runway and may either detect a runway from another airport or misinterpret image features as a runway [24].

In contrast, DME measurements are available much earlier in the approach and continuously contribute to the filter. Their integration enhances aircraft pose estimation and stabilizes the computation of both lateral and longitudinal deviations, as shown in Fig. 16. Overall guidance performance, presented in the same figure, compares estimated localizer and glide deviations against ground truth. Across all flights, estimation errors remain below 2 m for the localizer and 1 m for the glide path, demonstrating the clear benefit of including DME measurements to improve inertial navigation and to compensate for missing or inaccurate visual data.

5 Conclusion

This paper presented a DME error model based on flight test data from an airliner, and its subsequent integration in a datafusion filter combined with inertial, air-data, and visual measurements. The proposed work introduced three key contributions. First, a comprehensive DME error model was formulated, combining nominal filtered noise and range dependant bias, with transient multipath effects, enabling more realistic, and less conservative, characterization of DME-based range measurements. Second, this paper presented a hybrid navigation and control framework combining DME, IRS, visual, and ADR sensors for robust aircraft guidance during approach and landing. Third, this model was integrated into a previously developed PBVS guidance framework [24], forming a unified estimation and control scheme validated

on a high-fidelity real-time simulation platform [25]. Simulation results demonstrated that incorporating DME measurements significantly enhances navigation continuity and accuracy, especially in degraded visual conditions or when false detections occur. Across multiple autonomous landings at Toulouse airport (LFBO), the hybrid filter maintained localizer and glide deviation errors below 2 m and 1 m respectively, confirming the benefits of multi-sensor fusion for resilient autonomous landing operations. Overall, the presented framework highlights the feasibility and operational interest of combining radio-navigation and vision-based approaches within an APNT context.

References

[1] Thorsten Schrader, Jochen Bredemeyer, Marius Mihalachi, David Ulm, Thomas Kleine-Ostmann, Christoph Stupperich, Sergei Sandmann, and Heyno Garbe. High-resolution signal-in-space measurements of vhf omnidirectional ranges using uas. *Advances in Radio Science*, 17(A.):1–10, 2019.

[2] Zaher M Kassas, Sharbel Kozhaya, Haitham Kanj, Joe Saroufim, Samer W Hayek, Mohammad Neinavaie, Nadim Khairallah, and Joe Khalife. Navigation with multi-constellation leo satellite signals of opportunity: Starlink, oneweb, orbcomm, and iridium. In *2023 IEEE/ION Position, Location and Navigation Symposium (PLANS)*, pages 338–343. IEEE, 2023.

[3] Sherman Lo, Yu Hsuan Chen, Per Enge, Benjamin Peterson, Robert Erikson, and Robert Lilley. Distance measuring equipment accuracy performance today and for future alternative position navigation and timing (apnt). In *Proceedings of the 26th International Technical Meeting of the Satellite Division of The Institute of Navigation (ION GNSS+ 2013)*, pages 711–721, 2013.

[4] Rudolph Emil Kalman. A new approach to linear filtering and prediction problems. 1960.

[5] Dan Simon. *Optimal state estimation: Kalman, H infinity, and nonlinear approaches*. John Wiley & Sons, 2006.

[6] Fredrik Gustafsson, Fredrik Gunnarsson, Niclas Bergman, Urban Forssell, Jonas Jansson, Rickard Karlsson, and P-J Nordlund. Particle filters for positioning, navigation, and tracking. *IEEE Transactions on signal processing*, 50(2):425–437, 2002.

[7] Mohinder S Grewal. Kalman filtering. In *International encyclopedia of statistical science*, pages 1285–1289. Springer, 2025.

[8] Pedro Batista, Carlos Silvestre, and Paulo Oliveira. Globally exponentially stable filters for source localization and navigation aided by direction measurements. *Systems & Control Letters*, 62(11):1065–1072, 2013.

[9] Lorenzo Fusini, Thor I Fossen, and Tor Arne Johansen. Nonlinear observers for gnss-and camera-aided inertial navigation of a fixed-wing uav. *IEEE Transactions on Control Systems Technology*, 26(5):1884–1891, 2017.

[10] Torleiv H Bryne, Jakob M Hansen, Robert H Rogne, Nadezda Sokolova, Thor I Fossen, and Tor A Johansen. Nonlinear observers for integrated ins\/gnss navigation: implementation aspects. *IEEE Control Systems Magazine*, 37(3):59–86, 2017.

[11] Tariqul Islam, Md Saiful Islam, Md Shajid-Ul-Mahmud, and Md Hossam-E-Haider. Comparison of complementary and kalman filter based data fusion for attitude heading reference system. In *AIP Conference Proceedings*, volume 1919, page 020002. AIP Publishing LLC, 2017.

[12] Michał Nowicki, Jan Wietrzykowski, and Piotr Skrzypczyński. Simplicity or flexibility? complementary filter vs. ekf for orientation estimation on mobile devices. In *2015 IEEE 2nd International Conference on Cybernetics (CYBCONF)*, pages 166–171. IEEE, 2015.

[13] RW Latham and PT Richards. A multi-dme/inertial system for aircraft positioning. *Navigation*, 24(1):72–83, 1977.

[14] John Charles Bobick and Arthur E Bryson Jr. Improved navigation by combining vor/dme information with air or inertial data. Technical report, 1972.

[15] Min Liu, Jizhou Lai, Zhimin Li, and Jianye Liu. An adaptive cubature kalman filter algorithm for inertial and land-based navigation system. *Aerospace Science and Technology*, 51:52–60, 2016.

[16] Omar García Crespillo, Anja Grosch, and Michael Meurer. Detection of dme ranging faults with ins coupling. In *2017 Integrated Communications, Navigation and Surveillance Conference (ICNS)*, pages 4B2–1. IEEE, 2017.

[17] Omar Garcia Crespillo, Anja Grosch, Elisabeth Nossek, Okuary Osechas, Boubeker Belabbas, and Michael Meurer. Integrated inertial navigation system with multiple apnt ranges: Expected performance and considerations. In *2016 Integrated Communications Navigation and Surveillance (ICNS)*, pages 3B3–1. IEEE, 2016.

[18] Birendra Kujur, Samer Khanafseh, Boris Pervan, Valeriu Vitan, Gerhard Berz, and Okuary Osechas. Integrated dme/ins alternative pnt system for rnp 1. In *Proceedings of the 38th International Technical Meeting of the Satellite Division of The Institute of Navigation (ION GNSS+ 2025)*, pages 1624–1646, 2025.

[19] Rohan Kapoor, Subramanian Ramasamy, Alessandro Gardi, and Roberto Sabatini. Uav navigation using signals of opportunity in urban environments: A review. *Energy Procedia*, 110:377–383, 2017.

[20] John F Raquet, Mikel M Miller, and Thao Q Nguyen. Issues and approaches for navigation using signals of opportunity. In *Proceedings of the 2007 National Technical Meeting of The Institute of Navigation*, pages 1073–1080, 2007.

[21] Zaher Zak M Kassas, Joe Khalife, Ali Abdallah, Chiawei Lee, Juan Jurado, Steven Wachtel, Jacob Duede, Zachary Hoeffner, Thomas Hulsey, Rachel Quirarte, et al. Assessment of cellular signals of opportunity for high-altitude aircraft navigation. *IEEE Aerospace and Electronic Systems Magazine*, 37(10):4–19, 2022.

[22] Frédéric Faurie. *Algorithmes de contrôle d'intégrité pour la navigation hybride GNSS et systèmes de navigation inertielle en présence de multiples mesures satellitaires défaillantes*. PhD thesis, Bordeaux 1, 2011.

[23] Yang Gao. A new algorithm of receiver autonomous integrity monitoring (raim) for gps navigation. In *Proceedings of the 4th International Technical Meeting of the Satellite Division of The Institute of Navigation (ION GPS 1991)*, pages 887–896, 1991.

[24] Sofiane Kraïem, Augustin Fuchs, Gustav Öman Lundin, Cédric Seren, and Mario Cassaro. A pose-based visual servoing strategy for the autonomous - landing of an airliner using a yolov11 model for runway. In *EUCASS2025-305 11 EUROPEAN CONFERENCE FOR AERONAUTICS AND SPACE SCIENCES (EUCASS)*, 2025. doi: DOI: 10.13009/EUCASS2025-305.

[25] Sofiane Kraïem, Cédric Seren, Aurélien Plyer, Gustav Öman Lundin, Mathieu Brunot, and Mario Cassaro. A real-time simulation environment for aircraft vision-based autonomous landing system design. In *2024 10th International Conference on Automation, Robotics and Applications (ICARA)*, pages 260–264. IEEE, 2024.

[26] Atsushi Kezuka, Takayuki Yoshihara, Susumu Saitoh, Takeyasu Sakai, and Naoki Fujii. Analysis of dme ranging error fluctuation caused by atmospheric delay to clarify ranging accuracy for apnt. In *Proceedings of the 27th International Technical Meeting of the Satellite Division of The Institute of Navigation (ION GNSS+ 2014)*, pages 3048–3054, 2014.

[27] Atsushi Kezuka, Takayuki Yoshihara, and Naoki Fujii. Raytracing analysis of dme ranging error variation due to atmospheric change. In *2017 International Symposium on Antennas and Propagation (ISAP)*, pages 1–2. IEEE, 2017.

[28] Kuangmin Li, Wouter Pelgrum, and Adam Naab-Levy. Impact of ground multipath on terrestrial radio navigation performance. In *Proceedings of the 26th International Technical Meeting of the Satellite Division of The Institute of Navigation (ION GNSS+ 2013)*, pages 722–736, 2013.

[29] Nicolas Schneckenburger, Uwe-Carsten Fiebig, Sherman Lo, Per Enge, and Robert Lilley. Characterization and mitigation of multipath for terrestrial based aviation radionavigation. *Navigation: Journal of The Institute of Navigation*, 65(2):143–156, 2018.

[30] Bernard Russel Bowring. Transformation from spatial to geographical coordinates. *Survey review*, 23(181):323–327, 1976.

[31] John Parker Burg. *Maximum entropy spectral analysis.* Stanford University, 1975.

[32] Sofiane Kraïem, Mario Cassaro, Cédric Seren, Aurélien Plyer, Gustav Öman Lundin, and Mathieu Brunot. A vision-based control solution for autonomous approach and landing of an airliner. In *CEAS EuroGNC 2024*, 2024.